Article

Relationships between Aerosols and Marine Clouds during the "Godzilla" Dust Storm: Perspective of Satellite and Reanalysis Products

Cheng-Hsiang Chang [1,*] and Farnaz Hosseinpour [1,2]

[1] Department of Physics, University of Nevada, Reno, NV 89557, USA; farnaz.hosseinpour@dri.edu
[2] Division of Atmospheric Sciences, Desert Research Institute, Reno, NV 89512, USA
[*] Correspondence: chenghsiangc@nevada.unr.edu

Abstract: In June 2020, a record-breaking Saharan dust storm, known as the "Godzilla" extreme event, caused significant dust transport from the Sahara Desert across the Atlantic Ocean to the United States. Based on satellite observations, the magnitude of aerosol optical depth (AOD) has consistently remained highest over the Atlantic Ocean for the past 18 years. This study uses satellite observations (including MODIS and CALIOP) and MERRA-2 reanalysis products to investigate the relationships between dust and marine clouds. During this extreme event, the concentration of AOD exhibits a synchronous anomaly with the cloud fraction (CF). Principal components analysis (PCA) results show that the enhanced temperature and specific humidity near the surface contribute the most to cloud development over the tropical Atlantic Ocean. Despite the reduced sensitivity of CF to aerosols, the semi-direct effect of dust can still play a crucial role during this extreme dust storm. We found that the presence of absorbing aerosols above the cloud layers warms the air, accompanied by an enhancement of surface moisture, thereby benefiting low-level cloud coverage.

Keywords: dust; dust storm; extreme event; aerosol–cloud interactions; satellite remote sensing

1. Introduction

Aerosol–cloud interactions still cause the most uncertainties for estimating radiative forcing in global climate models [1]. Dust is the most abundant aerosol type by mass [2,3], and understanding its radiative effects is crucial for reducing the uncertainty of model simulations. Dust aerosols could impact climate directly by absorbing or scattering energy from solar and terrestrial radiation [4–6]. They could also impact climate indirectly by serving as cloud condensation nuclei (CCN) [7–9]. The indirect effect of aerosols can enhance cloud albedo via decreasing cloud droplet size [10,11] and may extend cloud lifetime by suppressing precipitation [12]. Rosenfeld et al. [13] showed that Saharan dust aerosols diminish precipitation in shallow clouds; meanwhile, Min et al. [14] suggested that enhanced CCN and ice nuclei (IN) elevated by strong updraft reduce convective precipitation. Moreover, Weinzierl et al. [8] indicated that high Saharan dust concentrations are related to CCN enhancement. In addition to the indirect effect, absorbing dust can change clouds by heating the atmosphere.

The semi-direct effect was originally discussed as absorbing aerosols embedded in the cloud layer that may yield a positive climate force due to cloud coverage decreasing [15]. Ackerman et al. [16] performed a large-eddy simulation modeling wintertime cumulus clouds over the tropical Indian Ocean. Their studies argued that absorbing aerosols, which heat the air in the cloud layer, can reduce relative humidity and suppress convection. Conversely, other studies suggest that for absorbing aerosols residing above the cloud layer, the low cloud could be enhanced, leading to a negative forcing [17]. The semi-direct effect would be notably influenced by the distance between the absorbing aerosol layers and the cloud top. Koch and Del Genio [18] proposed that absorbing aerosols above the cloud top

might promote the formation of stratocumulus clouds, a type of warm cloud, by stabilizing the air below. This semi-direct effect indicating low cloud enhancement has been verified by simulations [17,19–22] and satellite observations [23–25]. While many studies focus on absorbing aerosols impacting cloud systems, such interactions under extreme weather conditions are not well understood.

A record-breaking extreme dust storm, called the "Godzilla" dust storm, harshly degraded the air quality in Puerto Rico [25] and transported dust aerosols to the southeastern United States in June 2020 [26]. Francis et al. [27] found that a wave train persisting in the northern hemisphere drove continuous dust emissions from the Sahara. In addition, the African easterly jet (AEJ), associated with the thermal contrast between the Saharan Desert and the Gulf of Guinea, contributed to the rapid dust transport. Pu and Jin [26] further pointed out that the intensified AEJ, the North Atlantic subtropical high, and the intensified Caribbean low-level jet favored the long-range transport of the Godzilla dust plume. Yu et al. [28] showed that the effect of intense haboobs sweeping through the Niger–Mali–Mauritania corridor was one of the driving factors for this unprecedented dust event. This event can serve as a natural experiment for studying the transport mechanisms and aerosol–cloud interactions associated with extreme weather.

This study investigates the influence of dust on low-level cloud cover during the "Godzilla" extreme dust storm by addressing two main questions: (1) how do the changes in the marine clouds relate to dust during this event, and (2) what are atmospheric and hydrological features contributing to cloud variation? To answer these questions, this study employs satellite observations and reanalysis products to investigate aerosol–cloud interactions associated with this extreme weather event.

2. Materials and Methods

2.1. Satellite Observations and Reanalysis

The moderate-resolution imaging spectroradiometer (MODIS) aboard the NASA Aqua satellite provides a horizontal resolution $1° \times 1°$ level-3 daily product of AOD [29], CF, and cloud effective radius (CER) [30]. The AOD dataset was obtained from the Dark-Target algorithm at 550 nm [31,32] to investigate the dust plume transported across the tropical Atlantic Ocean. Similarly, this study utilized the CER in the liquid phase (CER-liquid) to investigate the drop size variations in low clouds.

The vertical profiles of aerosols and clouds were investigated using the level-2 data from the Cloud-Aerosol Lidar with Orthogonal Polarization (CALIOP) instrument onboard the Cloud-Aerosol Lidar and Infrared Pathfinder Satellite Observation (CALIPSO) mission [33,34]. The data utilized in this study have a spatial resolution of 5 km $\times$ 60 m, which is derived from counting aerosol or cloud fractions within a grid of 1/3 km $\times$ 30 m. As a result, the maximum value of the level-2 layer fraction within the grid is 30. This study weighed the aerosol height with the corresponding layer fraction to yield the average height for a specified time and space segment. Aerosol average height $\langle H_{aer} \rangle$ is defined as:

$$\langle H_{aer} \rangle = \frac{\sum_{i \in s,t} f_{aer}(i) \cdot H_{aer}(i)}{\sum_{i \in s,t} f_{aer}(i)}, \tag{1}$$

where f_{aer} is the layer fraction of aerosols from the level-2 CALIOP data, t represents the time range, s stands for the specified space domain, and i is the datapoint within the assigned space–time range. Our study applied the same method for evaluating cloud vertical changes.

To examine the atmospheric anomalies, we used the Modern-Era Retrospective Analysis for Research and Applications, version 2 (MERRA-2) [35]. The daily average of wind, temperature, and specific humidity were calculated from the 3 hourly MERRA-2 data with a $0.625° \times 0.5°$ horizontal resolution and 42 vertical layers. We applied bilinear interpolation to co-locate MERRA-2 data with the grid points ($1° \times 1°$) of the MODIS observations.

2.2. Anomalous Conditions

We analyzed the anomalous atmospheric patterns during the Godzilla dust outbreak from 14 June to 25 June 2020, with respect to the climatology of the same time period from 2003 to 2019. This study also investigated the evolution of this extreme event by composing data every three days, resulting in so-called "states" as aerosols propagated toward the west. For example, the composite of the first three days is referred to as state 1, and the same rule applies to the following three-day periods. Accumulating the validated data from a state (three days) allowed this study to conduct statistical analysis using remote sensing observations.

To address aerosol–cloud interactions during this extreme dust event, we examined the high-loaded aerosol domain over the Atlantic Ocean (85° W–15° W, 10° N–25° N). We divided the area into seven regions, each spanning 10 degrees longitude and covering identical latitudes, for two reasons. First, we utilized each region to study the spatial evolution of this extreme event. Second, the regional dynamical factors impacting the interactions between aerosols and clouds might vary across West Africa, the tropical Atlantic Ocean, and the Caribbean islands. Table 1 gives detailed spatiotemporal settings for this study.

Table 1. Temporal and spatial scope of the analysis capturing the evolution of the 'Godzilla' dust extreme event.

Region	G	F	E	D	C	B	A
Lat (N)	10–25	10–25	10–25	10–25	10–25	10–25	10–25
Lon (W)	85–75	75–65	65–55	55–45	45–35	35–25	25–15
State		1		2		3	4
Time range		14 June 2020 ↓ 16 June 2020		17 June 2020 ↓ 19 June 2020		20 June 2020 ↓ 22 June 2020	23 June 2020 ↓ 25 June 2020

2.3. Principal Components Analysis (PCA)

Principal component analysis (PCA) is a statistical method widely used to retrieve data structures contributing to the covariance of a system. The eigenvectors derived from the covariance matrix are the principal components (PCs), and the explained variance ratios are the corresponding eigenvalues divided by the summation of all. The order of PCs is sorted by the explained variance ratios, and the modes of interest can be derived by projecting the system on the PCs. PCA capturing of spatial patterns and temporal compositions of one variable, which are referred to as empirical orthogonal function (EOF), has been widely applied to numerous climate studies such as El Niño–Southern Oscillation [36–38], Madden-Julian Oscillation [39,40], and North Atlantic Oscillation [41,42]. PCA has also been used in characterizing aerosol profiles [43–45] and air pollution [46,47].

This study utilized PCA to explore the covariance of atmospheric parameters associated with the cloud variations during the Godzilla dust storm. We estimated the correlation coefficients between the input variables and CF before performing PCA. The PC results show the quantitative and qualitative properties of each parameter varying with CF. Meanwhile, the modes indicate their spatial and temporal influence as the Godzilla dust storm struck the tropical Atlantic Ocean.

3. Results and Discussion

3.1. Climatology and Dust Outbreak

The climatology and anomalies of AOD, CF, and winds at 850 hPa were studied for the 12 days of the Godzilla event (Figure 1). The AOD climatology has a prominent pattern that initiates at the West African coast and extends toward the Caribbean basin (Figure 1a), while the clouds cover the tropical Atlantic Ocean (Figure 1b). The winds and

AOD anomalies (Figure 1c) show that the aerosol enhancement over the tropical Atlantic Ocean (blue box) coincides with the increased CF over the tropical Atlantic Ocean. The climatology and anomalies of temperature and specific humidity profiles associated with AOD and CF variation are given in Figure S1. The following part of the study focuses on the evolution of aerosols and clouds over the regions with the prominent AOD anomaly (blue box in Figure 1c).
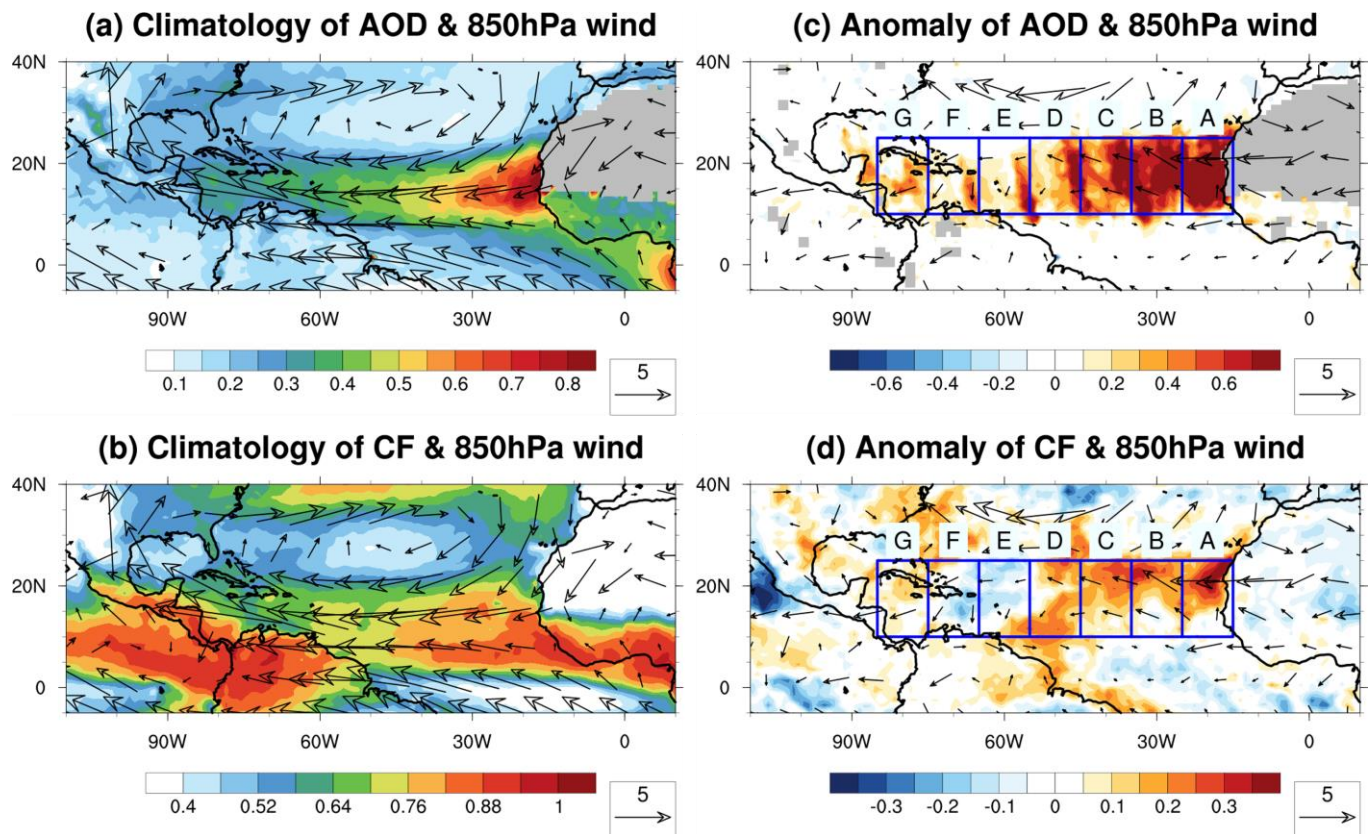

Figure 1. Climatology analysis of (**a**) AOD (shading) and (**b**) CF (shading) with accompanying 850 hPa wind (vectors; ms^{-1}); anomaly analysis of (**c**) AOD (shading) and (**d**) CF (shading) accompanied by 850 hPa wind anomaly (vectors; ms^{-1}). The climatology was calculated over the period of 14–25 June from 2003 to 2019. The anomalies are then compared to the corresponding period during the dust event in 2020, relative to the established climatology. The gray areas indicate missing values in the MODIS observation. The labeled blue boxes shown in (**c**) and (**d**) are the regions of interest for tracking the evolution of dust plumes. The spatial extent of each region can be found in Table 1.

3.2. Westward Transport of Warming and Convective Systems

Figure 2a–h show the evolution of the dust storm in each time state. The aerosol transport in each state coincides with the warm core moving westward during the development of the Godzilla dust storm. Meanwhile, the enhanced AOD is accompanied by mid-level anti-cyclonic wind anomalies in each state, propagating westward (Figure 2e–h). Hosseinpour and Wilcox suggested that AOD enhancement over the tropical Atlantic Ocean might be associated with the strength of anti-cyclonic vorticity based on their analysis of 13 years of satellite data [48].
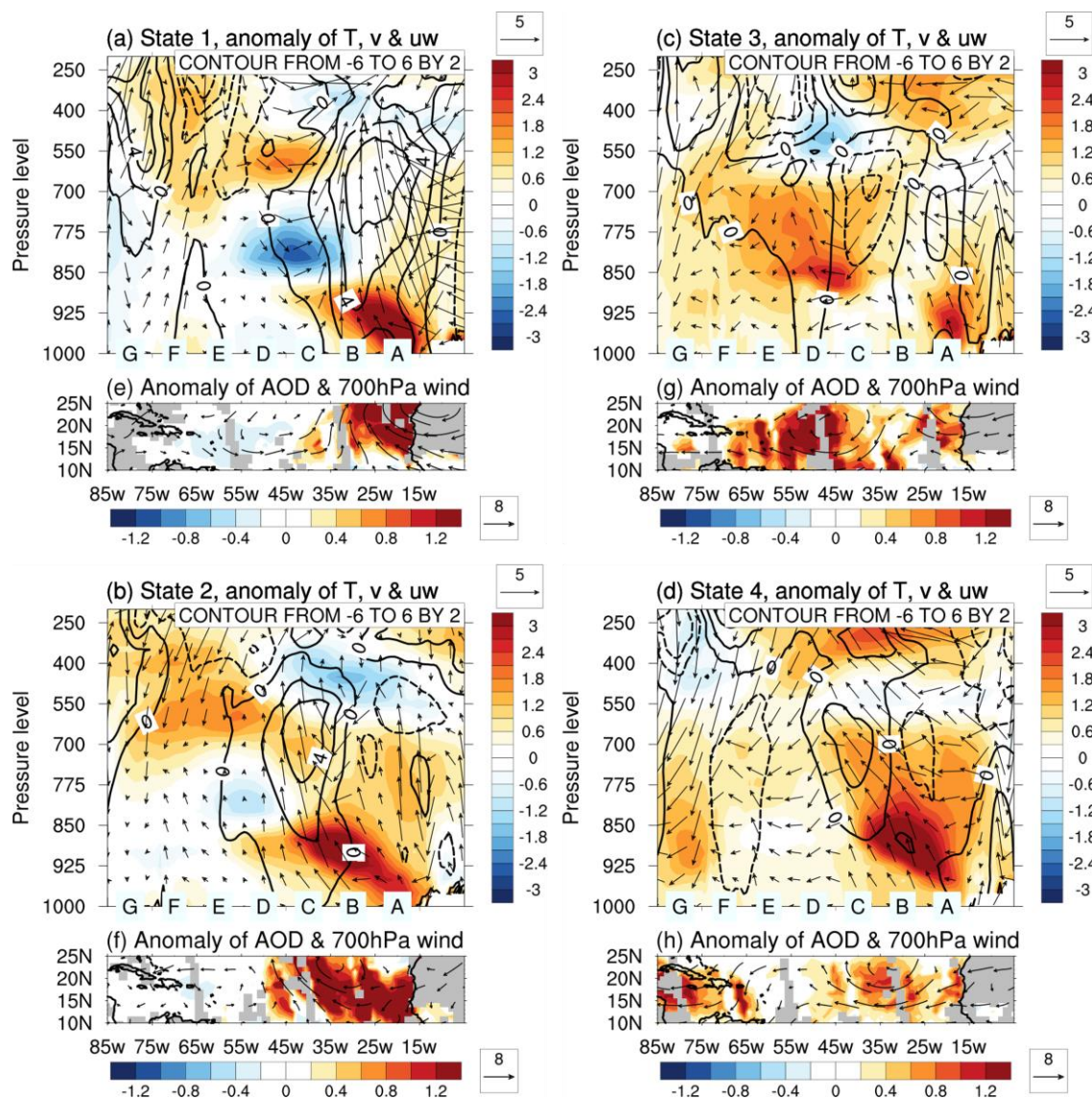
Figure 2. (**a**–**d**) Meridional anomaly of temperature (T, shading; K), v-wind (contour; ms^{-1}), and $u \times -100\omega$ wind (vector; ms$^{-1} \times$ Pas^{-1}) profiles and (**e**–**h**) AOD and 700 hPa wind anomaly. The profiles of anomalies are meridionally averaged from 10° to 25° N. The climatology analysis of the temperature profile and AOD can be found in Figure S1a,e, respectively.

In state 1, the upstream warm core (Figure 2a) corresponds to the high dust AOD originating from West Africa (Figure 2e), where the enhanced convection causes ascending airflow (Figure 2a). In state 2, the warm core, accompanied by the transported aerosols, is observed to shift to higher altitudes, extending up to 850 hPa (Figure 2b,f). This vertical displacement of the warm core is attributed to the anomalous updraft in mesoscale convection, which is associated with the African Easterly Waves (AEWs), as discussed by Hosseinpour and Wilcox [48]. In state 3, the enhanced AOD, located within the anti-cyclonic anomalies, continues to propagate further downstream when the warm core is observed to shift upward toward the middle layers (Figure 2c,g). Simultaneously, the second wave initiates over the west coast of Africa and coincides with the intensified warm updraft generated by the convection upstream. In state 4, the first aerosol concentration and the warm core reach the Caribbean islands (region G; Figure 2d,h). The aerosols embedded in the second wave are propagated further west, coinciding with the anti-cyclonic anomalies. The syn-

chronized movement of the aerosols and the warm core implies that the light-absorbing dust is elevated and heats the atmosphere during this event (Figure S2).

The elevated aerosols and the associated warming vary with the cloud enhancement coupling with the convective systems during the Godzilla event (Figure 3). In state 1, the enhanced CF coincides with the transient anti-cyclonic anomalies of the waves offshore (Figure 3e). The baroclinic instability of the waves is related to the intensified meridional anomalies over the eastern tropical Atlantic Ocean (contour core in Figure 3a; Hosseinpour and Wilcox, 2023 [49]). In addition, the moisture increase extends above 600 hPa, accompanied by enhanced updraft and cloudiness over the offshore region (Figure 3a,e). An enhancement of lower-level moisture is developed in areas B and C (Figure 3a). In state 2, the downstream development of CF is transported westward along with the convective systems (Figure 3b,f). Likewise, the enhanced moisture column coinciding with the propagation of the wave (the core of contours in Figure 3a,b) reaches to the west (region C). In state 3, the CF increase accompanied by the anti-cyclonic anomalies reveals a synchronized variation with dust concentration (Figures 2g and 3g). The increase in low-level moisture covers the tropical Atlantic Ocean, while a second wave system and elevated water vapor initiate in region A (Figure 3c). Finally, the anomalous subsidence associated with drier air over the Caribbean islands (Figure 3d) coincides with the dust AOD shown in Figure 2d. This subsidence is linked to the suppression of baroclinic instability during the dissipation of the wave. Meanwhile, the second convective system moves with the CF enhancement and the elevated water vapor to region C (Figure 3d,h).
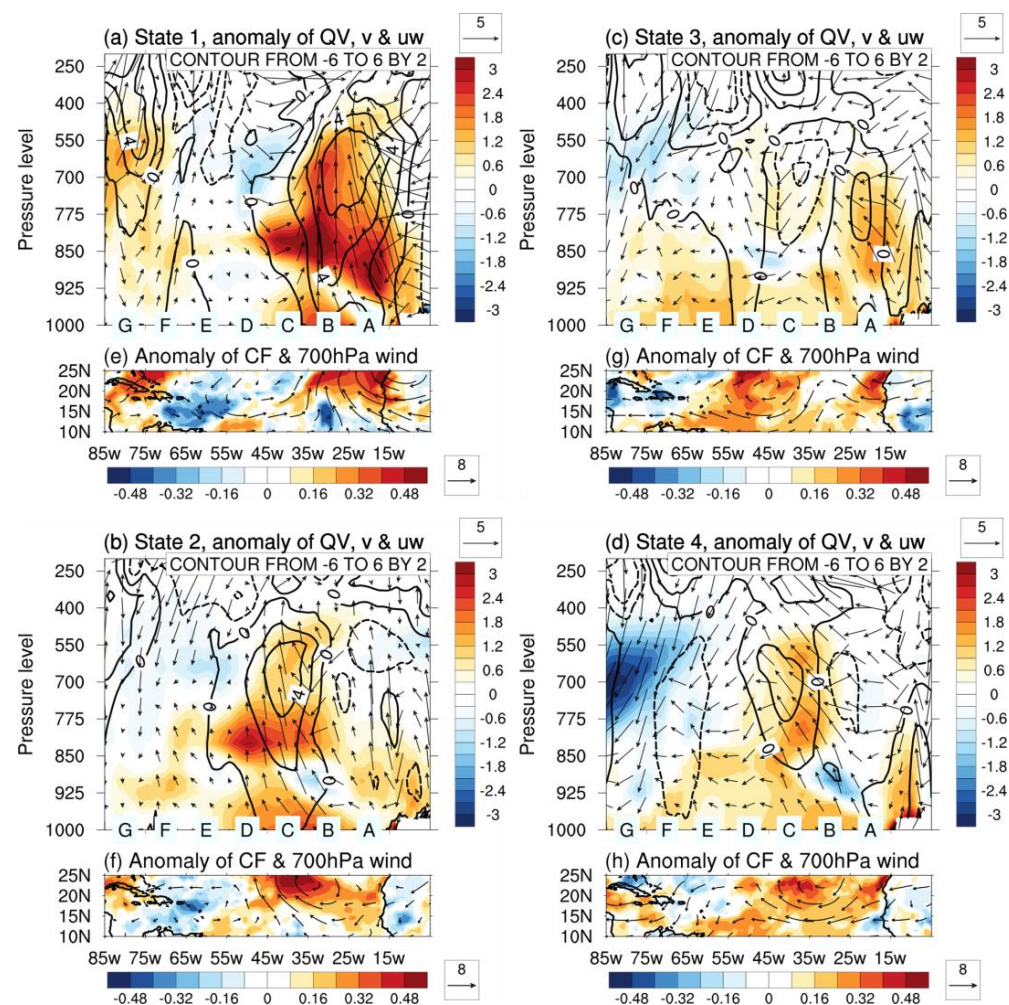

Figure 3. Same as Figure 2, but the anomaly of (**a**–**d**) specific humidity (QV, shading; g kg^{-1}) profiles and (**e**–**h**) CF (shading). The corresponding climatology analysis results are given in Figure S1b,f.

3.3. PCA Results and AOD-CF Relationships

In this section, PCA is applied to examine the systematic relationships between CF and the associated atmospheric parameters across the tropical Atlantic Ocean. In our study, we used the surface pressure (PS) and 10-m winds (U10M and V10M) to investigate the dynamic influence from the surface; 10-m temperature (T10M) and specific humidity (QV10M) were used to study the low-level thermal effect. We also examine the atmospheric impacts from the middle layer, specifically at 700 hPa. This level is significant as the jet weakens, facilitating the westward propagation of AEWs [50]. Moreover, our study identifies the prominent temperature anomaly at 700 hPa, which is associated with the anti-cyclonic anomalies shown in Figure 2. Thus, the selected parameters are geopotential height (H700), omega (ω700), u-wind (U700), v-wind (V700), temperature (T700), and specific humidity (QV700). AOD is utilized to study the effect of the aerosol column.

As the initial step, we estimate correlations between CF and the aforementioned atmospheric parameters. This analysis allows us to examine the covariance between cloud cover and the surrounding environmental conditions. The correlation coefficients are estimated for each space–time range (Table 1), and the preliminary results are presented individually in Figure S3. Subsequently, PCA is applied to derive contributing atmospheric variables that show representative space–time patterns affecting the Atlantic clouds while the extreme event evolved.

The most symbolic distribution of the first mode (Figure 4) has the highest explained variance ratio (44.7%). This space–time pattern represents the dominance of the strong convection offshore West Africa. In state 1, the intensified PS and H700, associated with the initiation of AEWs, are beneficial for cloud coverage. In state 2, the convection system moves toward the middle of the tropical Atlantic Ocean. Later, another, but weaker, dust plume initiates at region A, yielding a positive signal in states 3 and 4. The negative components of T10M and Q10M in PC1 and the negative signals over the middle tropical Atlantic Ocean suggest that the warm temperatures associated with dust (Figure 2a–e) and the moisture from the lower levels (Figure 3a–e) are favorable for promoting clouds but may not have benefited CF offshore of Africa. Similarly, the positive element of U700 in PC1 shows the importance of easterlies to marine CF, where these winds are also responsible for aerosol transport. The second representative mode, which has an explained variance ratio of 24.9%, exhibits a significant westward propagation racing toward the Caribbean islands (Figure 5). This signal reveals a westward systematic effect, and the component feature from PC2 suggests a positive relationship between cloud variation and enhanced PS, AOD, and temperature at 700 hPa (T700). The negative atmospheric variables of PC2 reveal the importance of surface easterlies and the decrease in specific humidity associated with the westward effect. Thus, the space–time pattern and the PC2 support the synchronic movement of anomalous anti-cyclone circulation and AOD (Figure 2). The negative tendency of QV correlation to CF may relate to anomalous airflow from higher levels containing less moisture (Figure 3a–d). The westward transportation observed during the Godzilla event might relate to the systematic influence of the AEJ, the North Atlantic subtropical high, and the intensified Caribbean low-level jet, as proposed by Pu and Jin [26]. The first two results from PCA contain more than half the explained variance.

While CF varies with atmospheric parameters westward (Figure 5), the impact of AOD is less pronounced when substantial dust, potentially acting as cloud condensation nuclei (CCN) or ice nuclei (IN), reaches the tropical Atlantic Ocean. In the following section, we analyze the relationship between CF and AOD during the Godzilla event for each state and region. Figure 6a,b display the average distribution of AOD and CF, respectively; the space–time relationships between CF and AOD are determined through linear regression analysis. The regression analysis (Figure 6c) suggests that a systematic effect of space and time suppresses cloud sensitivity to Saharan dust. We note that the responses of cloud coverage to aerosols are still positive, but CF sensitivity to AOD becomes lower. The suppression can reach downstream in state 3 when AOD synchronically arrives in the Caribbean islands. One of the plausible reasons is that the increase in dust might not have

facilitated more cloud formation in already cloudy conditions. Under this situation, the surface easterlies and the warming air at 700 hPa are more significant for clouds' westward propagation in the Godzilla case (Figure 5).
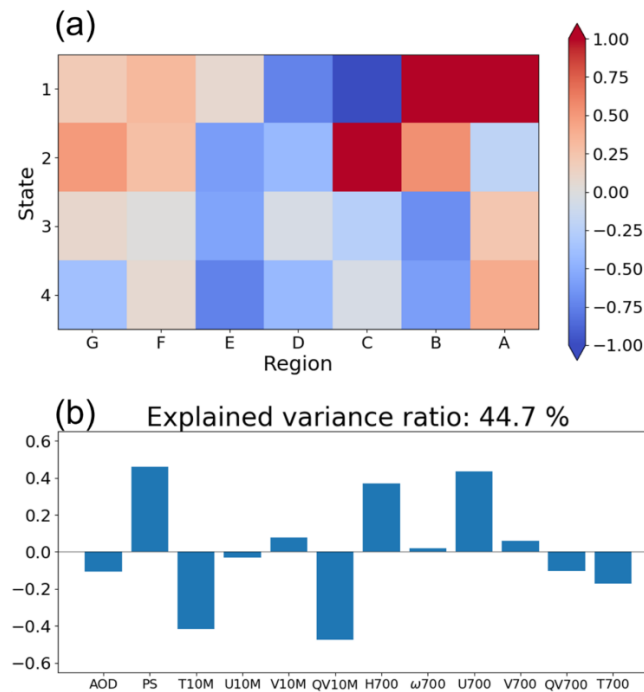

Figure 4. The first mode (**a**) and the corresponding PC (**b**) obtained from PCA have an explained variance ratio of 44.7%. The top panel displays the space–time pattern of the first mode. The bottom panel shows the contribution of each variable to PC1. The inputs used for PCA are the correlation coefficients between the corresponding meteorological variables noted in the bottom panel with cloud fraction (CF).
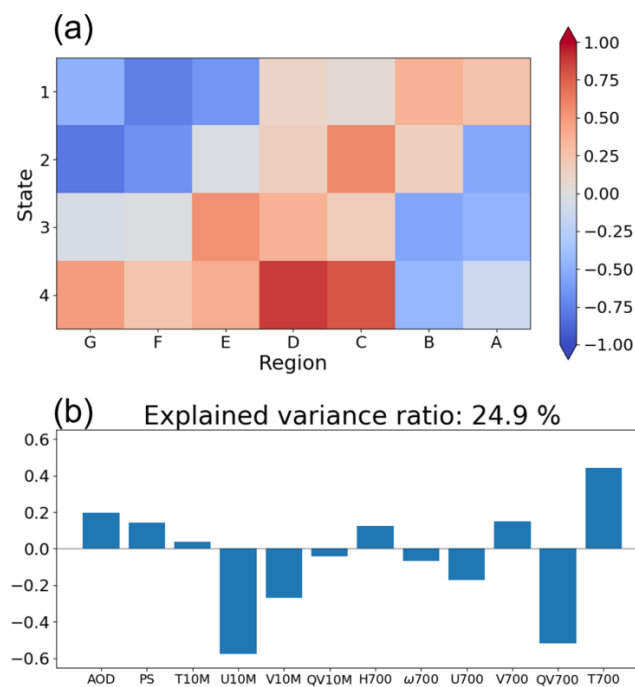

Figure 5. Same as Figure 4, but for the second mode (**a**) and its PC (**b**), obtained from PCA with an explained variance ratio of 24.9%.
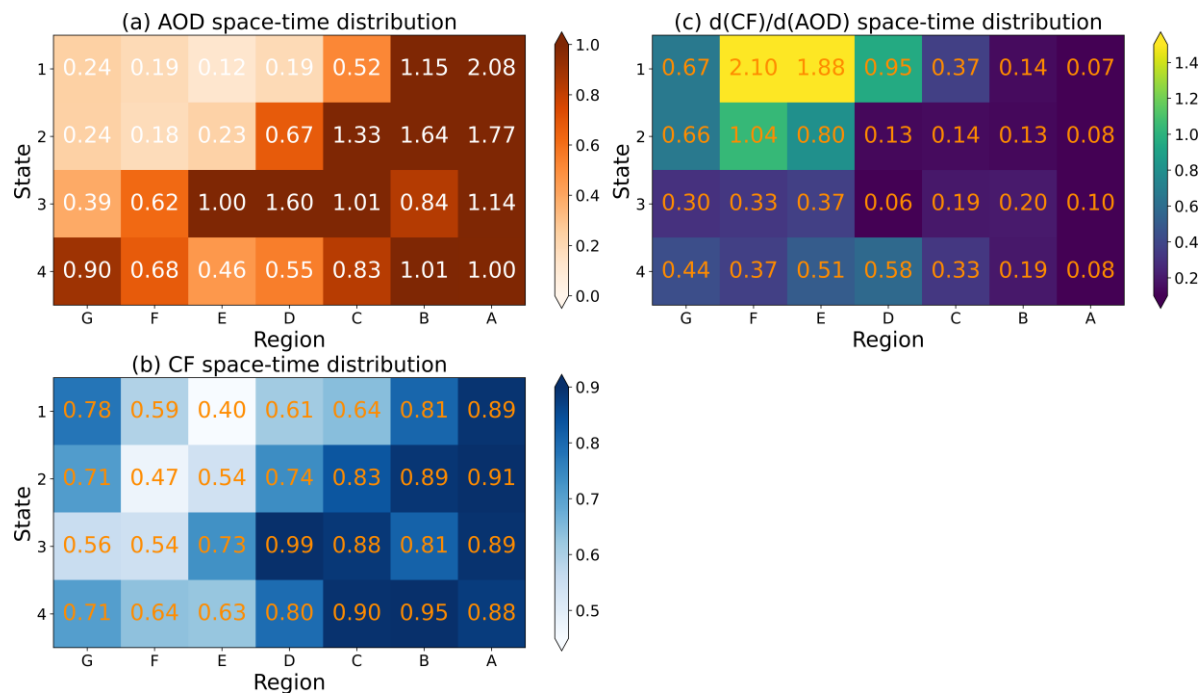
Figure 6. Space–time distribution of (**a**) AOD, (**b**) CF, and (**c**) the derivatives of CF to AOD. The space–time of the AOD and CF distributions are derived from averaging data over each region and time given in Table 1. The derivatives shown in (**c**) are obtained via the linear regression of CF to AOD. The p-values of the derivatives in (**c**) are less than 0.005.

3.4. Evolution of Aerosols and Clouds during the Extreme Dust Storm

This section focuses on the altitude changes of aerosols and clouds in space and time during the Godzilla dust storm. The CALIOP profiles in each region and state (Table 1) and Equation (1) are used to derive the average height of aerosols and clouds shown in Figure 7a and 7b, respectively. The aerosol average height reaches an altitude higher than 3 km offshore West Africa (regions A; Figure 7a). While the dust aerosols are transported westward, the average height of aerosols ascends, and the elevated dust can reach the western tropical Atlantic Ocean (regions F and G) in state 4. In addition, the average height of aerosols descends toward the west. Thus, the space–time distribution of aerosol layers represents a gradient. This observed result implies that the SAL embedded with dust lowers during the dust storm. The average height of clouds reveals that higher clouds dominate in the western tropical Atlantic Ocean (Figure 7b). The low clouds (<2 km) are located near the West African offshore and propagate westward with the dust transport (Figure 7c).

This study also examines the vertical variations in the microphysical properties of low clouds in relation to moisture changes associated with the dust storm. We have applied linear regression to the CER in the liquid phase (CER-liquid) and AOD, but the high p-values indicate the complexity of the microphysical processes involved in this case (not shown). Instead, we calculate the average QV from 1000 hPa to 600 hPa for every 100 hPa as an interval containing the up and the bottom limits. Subsequently, the space–time correlations between the QV layers and CER-liquid are obtained and presented in Figure 8. In state 1, the high correlations between the CER-liquid and the QV are located offshore West Africa (regions C–A), especially at lower levels (<800 hPa). In the next state, the convection system moves westward and pumps up QV (Figure 3b). The hotspot of the correlations propagates westward and reaches 700 hPa (Figure 8b). In addition to the hotspot movement, the correlations between the low-level QV and CER-liquid over the western tropical Atlantic Ocean are developed in state 3 (Figure 8c) when the signal of the warm cloud increases and reaches region G (Figure 7c). Figure 8d shows that the high

correlations arrive at 600 hPa, and the hotspots are associated with the convection initiated by another dust plume (Figures 2d and 3d). These findings indicate that the relationship between CER liquid and water vapor propagates westward. The finding agrees with the hypothesis that providing sufficient water vapor can promote the growth of cloud droplets when aerosols mix with clouds [51].
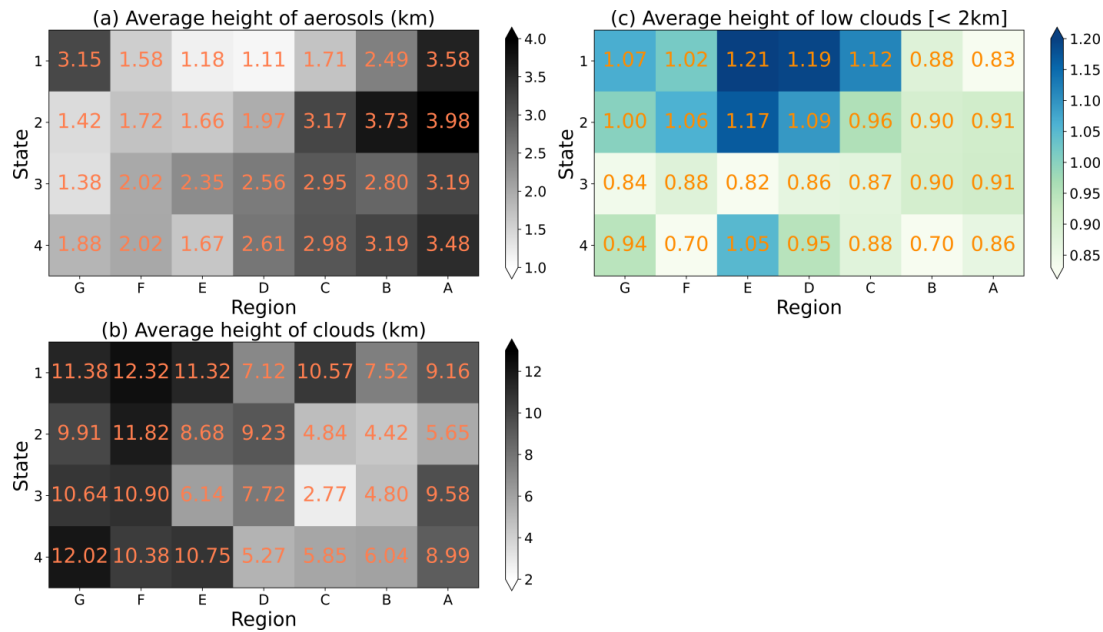

Figure 7. Average height of (**a**) aerosols, (**b**) clouds, and (**c**) low clouds (<2 km). The average height in each state and region (Table 1) is derived by applying Equation (1) to the layer fraction obtained from CALIOP level-2 observations.
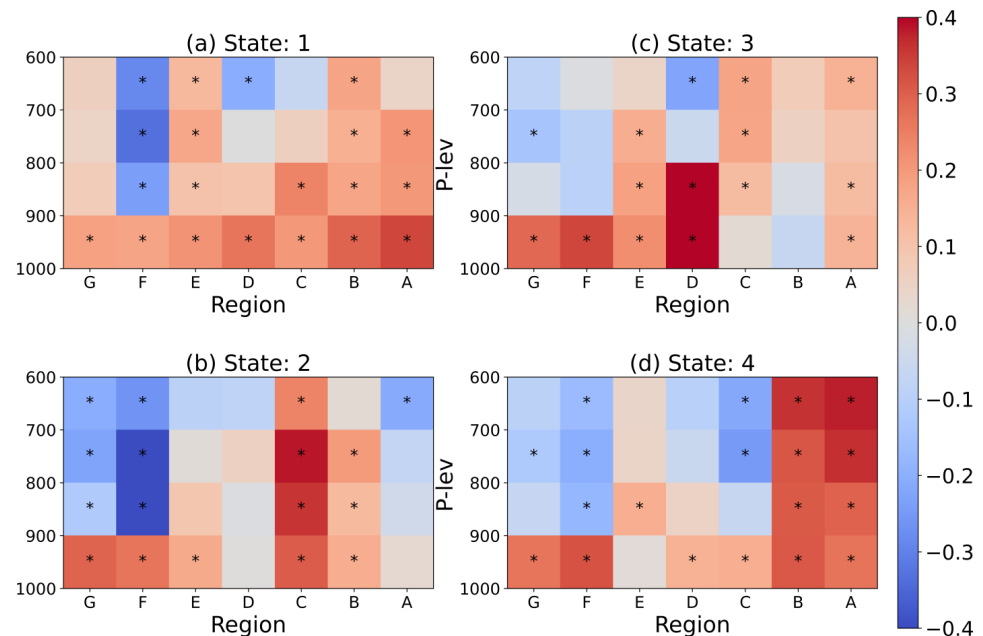

Figure 8. Correlations between CER in the liquid phase (CER-liquid) and different layers' specific humidity (QV) from state 1 to state 4 (**a**–**d**). The vertical QV is averaged across each 100 hPa interval, ranging from 1000 hPa to 600 hPa, inclusive of both the upper and lower limits. The results are obtained from correlation analysis between CER-liquid and the QV layers for each state and region (as shown in Table 1). The asterisks (*) indicate that the corresponding Pearson's *r*-values are below the significance threshold of 0.05.

3.5. Vertical Characteristics of SAL Using CALIOP Observations

Figure 9 displays the vertical distribution of the aerosol layer fraction, cloud layer fraction, and anomalies of temperature and specific humidity during the Godzilla dust storm. The CALIOP profiles exhibit that the altitude of the elevated Saharan Air Layer (SAL) is reduced across the tropical Atlantic Ocean. In the beginning (state 1), the aerosols reach higher than 5 km at region A (offshore West Africa), while this height is reduced to around 2 km close to the western Atlantic Ocean (region G). These results also show an altitude gradient that agrees with the average height of aerosols shown in Figure 7a. Noteworthy, at the end (state 4), the top of aerosol fractions rises to approximately 4 km over the western tropical Atlantic Ocean (region G) and to about 6 km offshore West Africa (region A). Some cloud fractions can extend to altitudes exceeding 8 km, which relates to the higher average height of clouds in regions G and F (Figure 8b). In the middle tropical Atlantic Ocean (regions C–E), the presence of low clouds, specifically those below 2 km in altitude, contributes to the observed decrease in average cloud height depicted in Figure 7b,c. In the upstream, the development of clouds is associated with offshore convection (Figure 3).
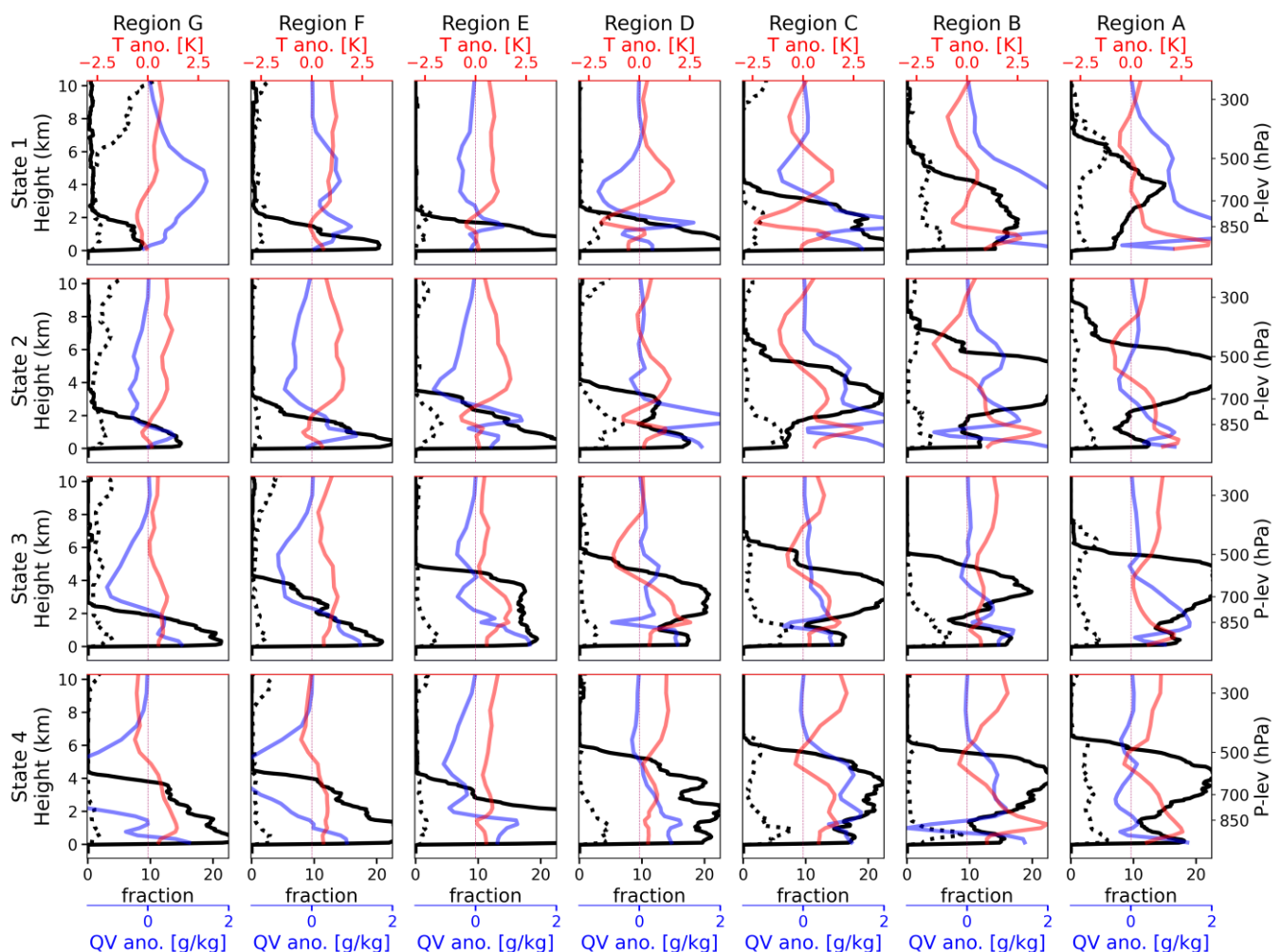

Figure 9. Profiles of aerosol layer fraction (solid black line), cloud layer fraction (dashed black line), anomalous temperature (T; red line), and anomalous specific humidity (QV; blue line). The thin vertical dashed line represents the zero anomaly of T and QV. The profiles of aerosol and cloud are obtained by averaging the CALIOP level-2 layer fraction for each state and region (Table 1).

Also, Figure 9 illustrates the environmental anomalies associated with the vertical distributions of aerosols and clouds during the dust storm. The cooling above 550 hPa,

shown in Figure 2a–d as well, might relate to the concentration of light-absorbing dust aerosols [48,52]. The cooling signals in Figure 9 are especially prominent in state 2 within regions A–C (same as Figure 2b), with altitudes closely matching the top of the dust clouds. When another plume develops in state 4, the cooling at 500 hPa can also be observed in regions A–C. Below 700 hPa, the warming is generally accompanied by anomalous ascending motion, which is embedded within SAL and is supported by Figure 2. Hosseinpour and Wilcox [49] proposed that heating from dust aerosols can enhance baroclinicity. For the layers lower than 850 hPa, in addition to the warming, Figure 9 shows the increase in QV (Figure 3) and the low clouds' layer fraction peak in regions B–E. The heating caused by the absorption of dust may have contributed to the increase in QV from the surface, facilitating the development of low clouds. This mechanism is consistent with the observed environmental anomalies during the Godzilla dust storm. From state 1 to state 2, the increases in low clouds in regions C–E are accompanied by the enhancement of QV near the surface. The westward propagation of low clouds can reach F–G in state 3, consistent with Figure 7c. In addition to more cloud coverage, the water vapor supply could increase the droplet size of liquid clouds (Figure 8). Moreover, Figure 9 reveals that certain low clouds reside beneath a peak of the aerosol fractions at higher altitudes. In state 2, regions B and C exhibit a peak of the aerosol fraction that extends higher than 2.5 km and above the cloud layer. In the next state, as the warming at 850 hPa (Figure 2c) shifts toward region D, the peaks of low clouds are apparent at regions B–D. In state 4, the low clouds still occupy the tropical Atlantic Ocean. The observational findings from CALIOP data are consistent with previous studies, suggesting that CF is enhanced when absorbing particles that reside above clouds [22,23,53].

4. Conclusions

In this study, we employed MODIS observations and the MERRA-2 reanalysis to investigate the relationships between aerosols, clouds, and environmental anomalies during the "Godzilla" extreme dust storm (14 June to 25 June 2020). Using the CALIOP observations, we have explored the vertical evolutions of the clouds and the aerosols within the Saharan air layer (SAL). These findings aim to provide insights into the aerosol–cloud interactions associated with extreme dust events.

During the Godzilla event, the intensified easterlies transport substantial aerosols, which coincides with the enhancement of cloud fraction (CF) over the tropical Atlantic Ocean. The dust moves with the warming, suggesting that the absorbing aerosols in the SAL heat the air during the dust storm. Meanwhile, the baroclinic instability and the elevated water vapor may have been linked to the dust concentration [49,54]. These findings demonstrate the relationships between changes in marine clouds and dust during this event, as well as the significant atmospheric and hydrological features associated with cloud variation.

This study employed PCA to investigate the crucial atmospheric parameters and their space–time patterns that contribute to the relationship between CF and the dust storm over the tropical Atlantic Ocean. Although the AOD-CF relationships are suppressed, the related atmospheric parameters still play a critical role in CF variation. PC1, which accounts for 44.7% of the explained variance, shows a significant influence of low-level temperature and moisture on CF over the ocean. PC2 exhibits a westward propagation pattern, explaining 24.9% of the variance. The influences of easterlies and temperature from PC2, which align with the movement of the warm core, exhibit a synchronic variation with CF. Our findings highlight the significance of the semi-direct effect of dust embedded in SAL in influencing CF during this extreme weather event.

Our analysis of CALIOP data indicates a gradient in aerosol height lowering towards the west, accompanied by an escalation of aerosol levels during the Godzilla dust storm. Meanwhile, an enhancement of low clouds is also observed over the tropical Atlantic Ocean when dust resides above the clouds. Combining with the MERRA-2 reanalysis, we find that warming within the aerosol layers and the supply of moisture from the lower levels

coincide with cloud fraction variations. These findings, derived from CALIOP observations, are consistent with our PCA results, indicating the significance of moisture supply from the surface and the transport of warming to CF variations.

It is important to acknowledge the limitations inherent in this study. This work, which applies remote sensing and reanalysis products for diagnostic analysis, cannot establish causality. Additionally, our study is unable to quantify the indirect and semi-direct effects of absorbing aerosols on CF enhancement, which will require further investigation. Building on the identified relationships between aerosols and marine clouds, we intend to employ regional climate models, such as the Weather Research and Forecasting (WRF) model coupled with chemistry, to provide more detailed insights into the physical effects caused by the dust particles. Sensitivity tests, such as tuning the absorption rate or dust emission rate [22], might help clarify this causality.

Supplementary Materials: The following supporting information can be downloaded at: https://www.mdpi.com/article/10.3390/atmos15010013/s1, Figure S1: Meridional climatology of v-wind (contour; ms^{-1}), $u \times -100\omega$ wind (vector; $ms^{-1} \times Pas^{-1}$), and (a) temperature (T, shading; K) and (b) specific humidity (QV, shading; $g\,kg^{-1}$); meridional anomaly of v-wind (contour; ms^{-1}), $u \times -100\omega$ wind (vector; $ms^{-1} \times Pas^{-1}$), and (c) temperature (shading; K) and (d) specific humidity (shading; gkg^{-1}). The climatology of 700 hPa wind and (e) AOD (shading) and (f) CF (shading); the anomaly of 700 hPa wind (vector; ms^{-1}) and (f) AOD (shading) and (g) CF (shading); Figure S2: (a–d) The evolution of aerosol shortwave radiative forcing (shading; $W\,m^{-2}$). The time range of states can be found in Table 1; Figure S3: Correlations between CF and the variables used in the PCA study.

Author Contributions: Conceptualization, C.-H.C. and F.H.; methodology, C.-H.C. and F.H.; software, C.-H.C.; validation, C.-H.C. and F.H; formal analysis, C.-H.C. and F.H.; investigation, C.-H.C. and F.H.; resources, C.-H.C. and F.H.; data curation, C.-H.C.; writing—original draft preparation, C.-H.C.; writing—review and editing, C.-H.C. and F.H.; visualization, C.-H.C.; supervision, F.H.; project administration, F.H.; funding acquisition, C.-H.C. All authors have read and agreed to the published version of the manuscript.

Institutional Review Board Statement: Not applicable.

Informed Consent Statement: Not applicable.

Data Availability Statement: Publicly available datasets were analyzed in this study. MODIS Aqua Level-3 of Collection 6.1 can be found here: https://ladsweb.modaps.eosdis.nasa.gov/archive/allData/61/MYD08_D3/ (accessed on 6 May 2022); the CALIPSO data can be found here: https://asdc.larc.nasa.gov/data/CALIPSO/LID_L2_05kmAPro-Standard-V4-20/ (accessed on 6 May 2022). The reanalysis data, MERRA-2, can be found here: https://disc.gsfc.nasa.gov/ (accessed on 6 May 2022).

Conflicts of Interest: The authors declare no conflict of interest.

References

1. Intergovernmental Panel on Climate Change. *Climate Change 2021—The Physical Science Basis*; Intergovernmental Panel on Climate Change: Geneva, Switzerland, 2023.
2. Hinds, W.C. *Aerosol Technology Properties, Behavior, and Measurement of Airborne Particles*; John Wiley & Sons: Hoboken, NJ, USA, 1999; Volume 14.
3. Kinne, S.; Schulz, M.; Textor, C.; Guibert, S.; Balkanski, Y.; Bauer, S.E.; Berntsen, T.; Berglen, T.F.; Boucher, O.; Chin, M.; et al. An AeroCom Initial Assessment—Optical Properties in Aerosol Component Modules of Global Models. *Atmos. Chem. Phys.* **2006**, *6*, 1815–1834. [CrossRef]
4. Auth Sokolik, I.N.; Toon, O.B. Direct Radiative Forcing by Anthropogenic Airborne Mineral Aerosols. *Nature* **1996**, *381*, 681–683. [CrossRef]

5. Tegen, I.; Lacis, A.A.; Fung, I. The Influence on Climate Forcing of Mineral Aerosols from Disturbed Soils. *Nature* **1996**, *380*, 419–422. [CrossRef]
6. Lau, K.M.; Kim, K.M. Cooling of the Atlantic by Saharan Dust. *Geophys. Res. Lett.* **2007**, *34*. [CrossRef]
7. Twohy, C.H.; Kreidenweis, S.M.; Eidhammer, T.; Browell, E.V.; Heymsfield, A.J.; Bansemer, A.R.; Anderson, B.E.; Chen, G.; Ismail, S.; DeMott, P.J.; et al. Saharan Dust Particles Nucleate Droplets in Eastern Atlantic Clouds. *Geophys. Res. Lett.* **2009**, *36*. [CrossRef]
8. Weinzierl, B.; Ansmann, A.; Prospero, J.M.; Althausen, D.; Benker, N.; Chouza, F.; Dollner, M.; Farrell, D.; Fomba, W.K.; Freudenthaler, V.; et al. The Saharan Aerosol Long-Range Transport and Aerosol-Cloud-Interaction Experiment: Overview and Selected Highlights. *Bull. Am. Meteorol. Soc.* **2017**, *98*, 1427–1451. [CrossRef]
9. Haarig, M.; Walser, A.; Ansmann, A.; Dollner, M.; Althausen, D.; Sauer, D.; Farrell, D.; Weinzierl, B. Profiles of Cloud Condensation Nuclei, Dust Mass Concentration, and Ice-Nucleating-Particle-Relevant Aerosol Properties in the Saharan Air Layer over Barbados from Polarization Lidar and Airborne in Situ Measurements. *Atmos. Chem. Phys.* **2019**, *19*, 13773–13788. [CrossRef]
10. Twomey, S. *Atmospheric Aerosols*; Elsevier Scientific Publishing Co.: New York, NY, USA, 1977.
11. Twomey, S.A.; Piepgrass, M.; Wolfe, T.L. An Assessment of the Impact of Pollution on Global Cloud Albedo. *Tellus B Chem. Phys. Meteorol.* **1984**, *36*, 356–366. [CrossRef]
12. Albrecht, B.A. Aerosols, Cloud Microphysics, and Fractional Cloudiness. *Science* **1989**, *245*, 1227–1230. [CrossRef]
13. Rosenfeld, D.; Rudich, Y.; Lahav, R. Desert Dust Suppressing Precipitation: A Possible Desertification Feedback Loop. *Proc. Natl. Acad. Sci. USA* **2001**, *98*, 5975–5980. [CrossRef]
14. Min, Q.L.; Li, R.; Lin, B.; Joseph, E.; Wang, S.; Hu, Y.; Morris, V.; Chang, F. Evidence of Mineral Dust Altering Cloud Microphysics and Precipitation. *Atmos. Chem. Phys.* **2009**, *9*, 3223–3231. [CrossRef]
15. Hansen, J.; Sato, M.; Ruedy, R. Radiative Forcing and Climate Response. *J. Geophys. Res. Atmos.* **1997**, *102*, 6831–6864. [CrossRef]
16. Ackerman, A.S.; Toon, O.B.; Stevens, D.E.; Heymsfield, A.J.; Ramanathan, V.; Welton, E.J. Reduction of Tropical Cloudiness by Soot. *Science* **2000**, *288*, 1042–1047. [CrossRef] [PubMed]
17. Johnson, B.T.; Shine, K.P.; Forster, P.M. The Semi-Direct Aerosol Effect: Impact of Absorbing Aerosols on Marine Stratocumulus. *Q. J. R. Meteorol. Soc.* **2004**, *130*, 1407–1422. [CrossRef]
18. Koch, D.; Del Genio, A.D. Black Carbon Semi-Direct Effects on Cloud Cover: Review and Synthesis. *Atmos. Chem. Phys.* **2010**, *10*, 7685–7696. [CrossRef]
19. Perlwitz, J.; Miller, R.L. Cloud Cover Increase with Increasing Aerosol Absorptivity: A Counterexample to the Conventional Semidirect Aerosol Effect. *J. Geophys. Res. Atmos.* **2010**, *115*. [CrossRef]
20. Sakaeda, N.; Wood, R.; Rasch, P.J. Direct and Semidirect Aerosol Effects of Southern African Biomass Burning Aerosol. *J. Geophys. Res. Atmos.* **2011**, *116*. [CrossRef]
21. Gordon, H.; Field, P.R.; Abe, S.J.; Dalvi, M.; Grosvenor, D.P.; Hill, A.A.; Johnson, B.T.; Miltenberger, A.K.; Yoshioka, M.; Carslaw, K.S. Large Simulated Radiative Effects of Smoke in the South-East Atlantic. *Atmos. Chem. Phys.* **2018**, *18*, 15261–15289. [CrossRef]
22. Ding, K.; Huang, X.; Ding, A.; Wang, M.; Su, H.; Kerminen, V.M.; Petäjä, T.; Tan, Z.; Wang, Z.; Zhou, D.; et al. Aerosol-Boundary-Layer-Monsoon Interactions Amplify Semi-Direct Effect of Biomass Smoke on Low Cloud Formation in Southeast Asia. *Nat. Commun.* **2021**, *12*, 6416. [CrossRef]
23. Wilcox, E.M. Stratocumulus Cloud Thickening beneath Layers of Absorbing Smoke Aerosol. *Atmos. Chem. Phys.* **2010**, *10*, 11769–11777. [CrossRef]
24. Adebiyi, A.A.; Zuidema, P. Low Cloud Cover Sensitivity to Biomass-Burning Aerosols and Meteorology over the Southeast Atlantic. *J. Clim.* **2018**, *31*, 4329–4346. [CrossRef]
25. Deaconu, L.T.; Ferlay, N.; Waquet, F.; Peers, F.; Thieuleux, F.; Goloub, P. Satellite Inference of Water Vapour and Above-Cloud Aerosol Combined Effect on Radiative Budget and Cloud-Top Processes in the Southeastern Atlantic Ocean. *Atmos. Chem. Phys.* **2019**, *19*, 11613–11634. [CrossRef]
26. Pu, B.; Jin, Q. A Record-Breaking Trans-Atlantic African Dust Plume Associated with Atmospheric Circulation Extremes in June 2020. *Bull. Am. Meteorol. Soc.* **2021**, *102*, E1340–E1356. [CrossRef]
27. Francis, D.; Fonseca, R.; Nelli, N.; Cuesta, J.; Weston, M.; Evan, A.; Temimi, M. The Atmospheric Drivers of the Major Saharan Dust Storm in June 2020. *Geophys. Res. Lett.* **2020**, *47*, e2020GL090102. [CrossRef]
28. Yu, H.; Tan, Q.; Zhou, L.; Zhou, Y.; Bian, H.; Chin, M.; Ryder, C.L.; Levy, R.C.; Pradhan, Y.; Shi, Y.; et al. Observation and Modeling of the Historic "Godzilla" African Dust Intrusion into the Caribbean Basin and the Southern US in June 2020. *Atmos. Chem. Phys.* **2021**, *21*, 12359–12383. [CrossRef]
29. Levy, R.C.; Mattoo, S.; Munchak, L.A.; Remer, L.A.; Sayer, A.M.; Patadia, F.; Hsu, N.C. The Collection 6 MODIS Aerosol Products over Land and Ocean. *Atmos. Meas. Tech.* **2013**, *6*, 2989–3034. [CrossRef]
30. Ackerman, S.A.; Holz, R.E.; Frey, R.; Eloranta, E.W.; Maddux, B.C.; McGill, M. Cloud Detection with MODIS. Part II: Validation. *J. Atmos. Ocean Technol.* **2008**, *25*, 1073–1086. [CrossRef]
31. Remer, L.A.; Kaufman, Y.J.; Tanré, D.; Mattoo, S.; Chu, D.A.; Martins, J.V.; Li, R.R.; Ichoku, C.; Levy, R.C.; Kleidman, R.G.; et al. The MODIS Aerosol Algorithm, Products, and Validation. *J. Atmos. Sci.* **2005**, *62*, 947–973. [CrossRef]
32. Remer, L.A.; Levy, R.C.; Mattoo, S.; Tanré, D.; Gupta, P.; Shi, Y.; Sawyer, V.; Munchak, L.A.; Zhou, Y.; Kim, M.; et al. The Dark Target Algorithm for Observing the Global Aerosol System: Past, Present, and Future. *Remote Sens.* **2020**, *12*, 2900. [CrossRef]
33. Winker, D.M.; Vaughan, M.A.; Omar, A.; Hu, Y.; Powell, K.A.; Liu, Z.; Hunt, W.H.; Young, S.A. Overview of the CALIPSO Mission and CALIOP Data Processing Algorithms. *J. Atmos. Ocean Technol.* **2009**, *26*, 2310–2323. [CrossRef]

34. Liu, Z.; Vaughan, M.; Winker, D.; Kittaka, C.; Getzewich, B.; Kuehn, R.; Omar, A.; Powell, K.; Trepte, C.; Hostetler, C. The CALIPSO Lidar Cloud and Aerosol Discrimination: Version 2 Algorithm and Initial Assessment of Performance. *J. Atmos. Ocean Technol.* **2009**, *26*, 1198–1213. [CrossRef]

35. Gelaro, R.; McCarty, W.; Suárez, M.J.; Todling, R.; Molod, A.; Takacs, L.; Randles, C.A.; Darmenov, A.; Bosilovich, M.G.; Reichle, R.; et al. The Modern-Era Retrospective Analysis for Research and Applications, Version 2 (MERRA-2). *J. Clim.* **2017**, *30*, 5419–5454. [CrossRef] [PubMed]

36. Kawamura, R. A Rotated EOF Analysis of Global Sea Surface Temperature Variability with Interannual and Interdecadal Scales. *J. Phys. Oceanogr.* **1994**, *24*, 707–715. [CrossRef]

37. Meyers, G. Variation of Indonesian Throughflow and the El Niño-Southern Oscillation. *J. Geophys. Res. Oceans* **1996**, *101*, 12255–12263. [CrossRef]

38. Wang, B.; An, S. Il A Method for Detecting Season-Dependent Modes of Climate Variability: S-EOF Analysis. *Geophys. Res. Lett.* **2005**, *32*. [CrossRef]

39. Kessler, W.S. EOF Representations of the Madden-Julian and Its Connection with ENSO. *J. Clim.* **2001**, *14*, 3055–3061. [CrossRef]

40. Wheeler, M.C.; Hendon, H.H. An All-Season Real-Time Multivariate MJO Index: Development of an Index for Monitoring and Prediction. *Mon. Weather. Rev.* **2004**, *132*, 1552–1574. [CrossRef]

41. Slonosky, V.C.; Jones, P.D.; Davies, T.D. Variability of the Surface Atmospheric Circulation over Europe, 1774–1995. *Int. J. Climatol.* **2000**, *20*, 1875–1897. [CrossRef]

42. Hurrell, J.W.; Deser, C. North Atlantic Climate Variability: The Role of the North Atlantic Oscillation. *J. Mar. Syst.* **2010**, *79*, 231–244. [CrossRef]

43. Chew, B.N.; Campbell, J.R.; Salinas, S.V.; Chang, C.W.; Reid, J.S.; Welton, E.J.; Holben, B.N.; Liew, S.C. Aerosol Particle Vertical Distributions and Optical Properties over Singapore. *Atmos. Environ.* **2013**, *79*, 599–613. [CrossRef]

44. Reid, J.S.; Kuehn, R.E.; Holz, R.E.; Eloranta, E.W.; Kaku, K.C.; Kuang, S.; Newchurch, M.J.; Thompson, A.M.; Trepte, C.R.; Zhang, J.; et al. Ground-Based High Spectral Resolution Lidar Observation of Aerosol Vertical Distribution in the Summertime Southeast United States. *J. Geophys. Res. Atmos.* **2017**, *122*, 2970–3004. [CrossRef]

45. Lu, Z.; Wang, J.; Chen, X.; Zeng, J.; Wang, Y.; Xu, X.; Christian, K.E.; Yorks, J.E.; Nowottnick, E.P.; Reid, J.S.; et al. First Mapping of Monthly and Diurnal Climatology of Saharan Dust Layer Height Over the Atlantic Ocean From EPIC/DSCOVR in Deep Space. *Geophys. Res. Lett.* **2023**, *50*, e2022GL102552. [CrossRef]

46. Statheropoulos, M.; Vassiliadis, N.; Pappa, A. Principal Component and Canonical Correlation Analysis for Examining Air Pollution and Meteorological Data. *Atmos. Environ.* **1998**, *32*, 1087–1095. [CrossRef]

47. Pandey, B.; Agrawal, M.; Singh, S. Assessment of Air Pollution around Coal Mining Area: Emphasizing on Spatial Distributions, Seasonal Variations and Heavy Metals, Using Cluster and Principal Component Analysis. *Atmos. Pollut. Res.* **2014**, *5*, 79–86. [CrossRef]

48. Hosseinpour, F.; Wilcox, E.M. Aerosol Interactions with African/Atlantic Climate Dynamics. *Environ. Res. Lett.* **2014**, *9*, 075004. [CrossRef]

49. Hosseinpour, F.E.; Wilcox, E.M. A New Look into the Impacts of Dust Radiative Forcing on the Energetics of Tropical Easterly Waves. *EGUsphere* **2023**, *2023*, 1–48. [CrossRef]

50. Kiladis, G.N.; Thorncroft, C.D.; Hall, N.M.J. Three-Dimensional Structure and Dynamics of African Easterly Waves. Part I: Observations. *J. Atmos. Sci.* **2006**, *63*, 2212–2230. [CrossRef]

51. Qiu, Y.; Zhao, C.; Guo, J.; Li, J. 8-Year Ground-Based Observational Analysis about the Seasonal Variation of the Aerosol-Cloud Droplet Effective Radius Relationship at SGP Site. *Atmos. Environ.* **2017**, *164*, 139–146. [CrossRef]

52. Spyrou, C.; Kallos, G.; Mitsakou, C.; Athanasiadis, P.; Kalogeri, C.; Iacono, M.J. Modeling the Radiative Effects of Desert Dust on Weather and Regional Climate. *Atmos. Chem. Phys.* **2013**, *13*, 5489–5504. [CrossRef]

53. Costantino, L.; Bréon, F.M. Aerosol Indirect Effect on Warm Clouds over South-East Atlantic, from Co-Located MODIS and CALIPSO Observations. *Atmos. Chem. Phys.* **2013**, *13*, 69–88. [CrossRef]

54. Lau, K.M.; Kim, K.M.; Sud, Y.C.; Walker, G.K. A GCM Study of the Response of the Atmospheric Water Cycle of West Africa and the Atlantic to Saharan Dust Radiative Forcing. *Ann. Geophys.* **2009**, *27*, 4023–4037. [CrossRef]